Comprehensive Density Functional Theory Studies of Vibrational Spectra of Carbonates

Yurii N. Zhuravlev [1] and Victor V. Atuchin [2,3,4,*

[1] Institute of Basic Sciences, Kemerovo State University, 650000 Kemerovo, Russia; zhur@kemsu.ru
[2] Research and Development Department, Kemerovo State University, 650000 Kemerovo, Russia
[3] Laboratory of Optical Materials and Structures, Institute of Semiconductor Physics, SB RAS, 630090 Novosibirsk, Russia
[4] Laboratory of Semiconductor and Dielectric Materials, Novosibirsk State University, 630090 Novosibirsk, Russia
* Correspondence: atuchin@isp.nsc.ru; Tel.: +7-(383)-3308889

Abstract: Within the framework of the density functional theory (DFT) and the hybrid functional B3LYP by means of the CRYSTAL17 program code, the wavenumbers and intensities of normal oscillations of $MgCO_3$, $CaCO_3$, $ZnCO_3$, $CdCO_3$ in the structure of calcite; $CaMg(CO_3)_2$, $CdMg(CO_3)_2$, $CaMn(CO_3)_2$, $CaZn(CO_3)_2$ in the structure of dolomite; $BaMg(CO_3)_2$ in the structure of the norsethite type; and $CaCO_3$, $SrCO_3$, $BaCO_3$, and $PbCO_3$ in the structure of aragonite were calculated. Infrared absorption and Raman spectra were compared with the known experimental data of synthetic and natural crystals. For lattice and intramolecular modes, linear dependences on the radius and mass of the metal cation are established. The obtained dependences have predictive power and can be used to study solid carbonate solutions. For trigonal and orthorhombic carbonates, the linear dependence of wavenumbers on the cation radius R_M (or M–O distance) is established for the infrared in-plane bending mode: $786.2–65.88·R_M$ and Raman in-plane stretching mode: $768.5–53.24·R_M$, with a correlation coefficient of 0.87.

Keywords: Density Functional Theory; normal vibrations; infrared spectra; Raman spectra; metal carbonates; cation radius

1. Introduction

Carbonates form an extensive class of chemical compounds containing the carbonate ion CO_3^{2-} as the main structural element [1,2]. In nature, carbonates are found in many minerals and play a crucial role in the carbon exchange of our planet [2–8]. Carbonate compounds are widely used in the construction industry, optics, and nanotechnology [9–15]. Appearance of the carbonate species due to chemical interaction with the atmosphere agents was detected at the surface of many oxide materials widely used in optical and electronic technologies [16–20]. In recent years, many artificial crystals of complex carbonates that have no analogues in nature were created [1]. Due to the specific features of the crystal structure, such materials, in many cases, are characterized by high birefringence, nonlinear optical properties, and transparency in the ultraviolet spectral range, which makes them perspective materials for use in optical devices in the UV range [21–27]. In this aspect, it is of particular importance to study the physicochemical properties of carbonates—in particular, the relationship between their structural and spectroscopic characteristics. According to this approach, this work is aimed at a systematic study of the relationship between the crystal structure and vibrational characteristics of a set of crystals of simple and binary anhydrous carbonates known in nature. Such minerals form several crystal-chemical families, which makes it possible to study the

effects of cation substitution on the wavenumbers of vibrational modes within the framework of a single structural type. In the near future, with the accumulation of experimental data of complex carbonates, this algorithm can be extended to new families of complex artificial crystals.

Natural carbonates are composed of over 60 minerals [2]. Simple and double rock-forming carbonates can be divided into three main groups based on the similarity of structures: calcite, dolomite, and aragonite. The structures of these crystals are shown in Figure 1. Calcite is the most abundant of all carbonate minerals [28]. The triangular geometry CO_3^{2-} dominates in the structure of calcite, which leads to rhombohedral symmetry of the crystal lattice with the space group *R-3c*. A primitive cell contains two formula units (*Z* = 2). Divalent cations are octahedrally coordinated by oxygen atoms (Figure 1a). The calcite group includes anhydrous carbonates with the general formula MCO_3 (M: Ca^{2+}, Mg^{2+}, Fe^{2+}, Zn^{2+}, Mn^{2+}, Co^{2+}, Ni^{2+} and Cd^{2+}): calcite ($CaCO_3$) [29], magnesite ($MgCO_3$) [30], siderite ($FeCO_3$) [31], smithsonite ($ZnCO_3$) [32], hodochrosite ($MnCO_3$) [33], spherocobaltite ($CoCO_3$) [34], gaspeite ($NiCO_3$) [35], and otavite ($CdCO_3$) [36]. The ability to form isomorphic mixtures is widespread among the minerals of the calcite series [37].
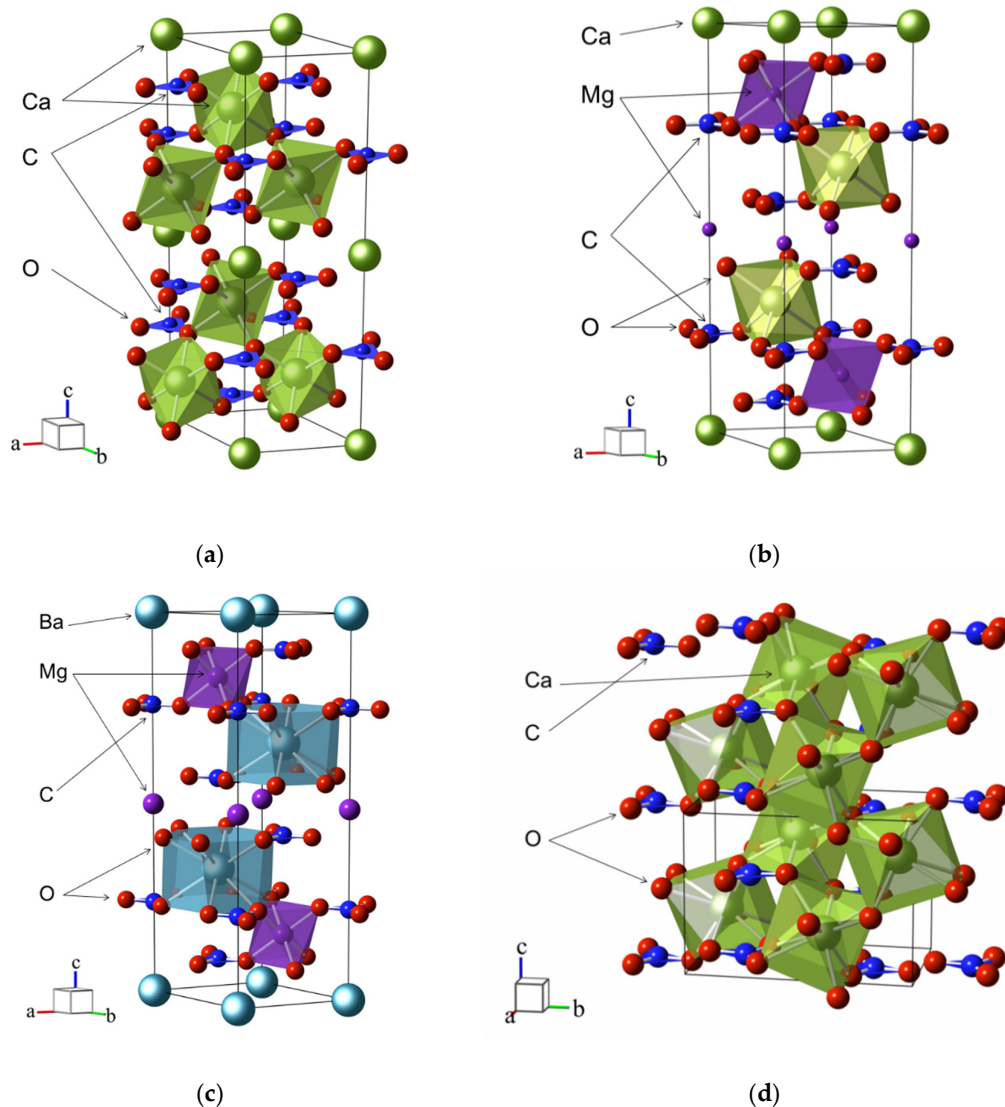

(a)

(b)

(c)

(d)

Figure 1. Fragments of the crystal structures of (**a**) $CaCO_3$ (calcite), (**b**) $CaMg(CO_3)_2$ (dolomite), (**c**) $BaMg(CO_3)_2$ (norsethite) and (**d**) $CaCO_3$ (aragonite) The unit cells are outlined. Lone atoms, excepting those in the unit cells, are omitted for clarity.

One of the most common minerals is a double carbonate—dolomite (CaMg(CO$_3$)$_2$) [38]. Dolomite is structured by natural minerals: minocordite (CaZn(CO$_3$)$_2$) [39], ankerite (CaFe(CO$_3$)$_2$) [40], and kutnohorite CaMn(CO$_3$)$_2$) [41]. Several crystals from the dolomite family were synthesized, including CdMg(CO$_3$)$_2$, CdMn(CO$_3$)$_2$, and CdZn(CO$_3$)$_2$ [42], and the structures were identified in [43]. Under ambient conditions, dolomite crystallizes in a rhombohedral structure with the space group *R*-3 (*Z* = 2). Its layered structure consists of alternating [CaO$_6$] and [MgO$_6$] octahedra separated by nearly flat and parallel carbonate groups. The structure differs from calcite by the absence of a slip plane.

Double carbonates are also known in the structure of norsethite (BaMg(CO$_3$)$_2$) [44] (Figure 1c). BaMn(CO$_3$)$_2$ does not exist in nature, but it was synthesized in [45]. The norsethite structure is described in *c*-space group *R*-3*c* symmetry with doubled *c*-axis, which corresponds to different rotations of carbonate groups [46]. As the temperature rises in BaMg(CO$_3$)$_2$, a phase transition is observed from a phase stable under ambient conditions to a high-temperature structure, which is accompanied by a change in the symmetry *R*-3*c* → *R*-3*m*. In the *R*-3*m* symmetry, the unit cell of BaMg(CO$_3$)$_2$ consists of the [MgO$_6$] octahedron, [BaO$_{12}$] polyhedron, and anions. Octahedra and polyhedra are in alternating layers, they are located exactly one above the other, parallel to the [001] direction and are separated by triangular groups CO_3^{2-}. Natural isostructural orthorhombic carbonates are aragonite (CaCO$_3$) (Figure 1d), strontianite (SrCO$_3$), cerussite (PbCO$_3$), and witherite (BaCO$_3$) [47,48], listed in the order of increasing the size of the cation. In a crystal structure with the space group *Pmcn* (*Z* = 4), layers of 9-coordinated cations M^{2+} (M: Ca^{2+}, Sr^{2+}, Pb^{2+}, Ba^{2+}) in an approximately hexagonal close packing alternate with layers of planar CO_3^{2-} groups arranged perpendicular to the *c*-axis. Like calcites, aragonites form solid solutions [49]. Studies of isostructural orthorhombic carbonates are important for understanding phase transition sequences under pressure and temperature and, therefore, can provide insight into a carbon behavior in the Earth mantle [50–53].

The optical properties of natural carbonates were extensively explored since these widespread and cheap natural minerals can be used as raw resources for infrared technology materials [54]. In this regard, their infrared spectra (IRS) [55] and Raman spectra (RS) [56,57] were previously studied experimentally and then theoretically [58,59]. Single crystals of iron-free magnesite were studied by Raman spectroscopy [30]; calcite and dolomite crystals were studied in [60] and all crystal were studied in [61]. In [62], they were evaluated with the methods of laser Raman spectroscopy and density functional theory (DFT) calculations using the plane wave basis (PW) and pseudopotentials of the Troullier–Martins type (TM PP). Otavite vibrational spectra were measured in experiment [63]. Eight natural carbonate minerals with a calcite structure were studied using Raman spectroscopy [64]. It was shown that changes in the wavenumber of phonon modes of the E_g(T) symmetry correlate with the distances between the nearest metal and oxygen atoms M–O and the cation ionic radii. Using a graphical approach, the authors developed the spectroscopic Raman model to calculate the ionic radius of a divalent metal cation present in a mineral.

In [65], studies of the infrared spectra of natural iron-free dolomite were carried out. A combined study of infrared absorption and Raman scattering on a natural dolomite sample CaMg$_{0.98}$Fe$_{0.02}$(CO$_3$)$_2$ was performed [66]. DFT using exchange correlation potentials in the local density approximation (LDA) and generalized gradient approximation (GGA) in the PW basis with TM PP were used here to interpret the obtained results. The Raman and infrared spectra of cerussite were measured and compared with the spectral characteristics of other minerals of the aragonite family [67]. RS and IRS at high temperature in situ were measured for aragonite, strontianite, cerussite, and witherite at atmospheric pressure [68]. Studies for high and medium temperature infrared absorption and Raman spectroscopy on a synthetic strontianite sample led to the construction of a pressure-temperature phase diagram [69]. In addition, here for the first time, the absorption spectra in the far infrared range were measured for the entire family of aragonite-type carbonates.

The works in which experimental and theoretical spectroscopic studies were performed for a group of carbonates with different structures are of particular interest. Thus, the purpose of the study [70] was to establish the influence of the M^{2+} cation type on the shift of positions of the absorption bands of various anhydrous carbonate minerals from the calcite and dolomite families. In this

contribution, it is shown that the position of the minima of absorption bands is unique for each chemical composition of carbonates and can be a diagnostic indicator in mineralogy. A selection of the frequencies of intramolecular modes for a large number of carbonates is also found in [71]. In [72], infrared spectra in the wavenumber range of 70–650 cm^{-1} were presented for 18 common and rare minerals which are quite pure in composition and have a known crystal structure. It is shown that the spectra in the far infrared range of different carbonates from the same structural group have a pronounced similarity, and the observed shifts demonstrate the effect of changing the mass of cations. The vibrational modes of natural minerals—aragonite, calcite, dolomite, magnesite, rhodochrosite, and siderite—that are active in the Raman spectrum were observed, and their pressure and temperature inducing frequency shifts were determined [73].

Thus, there are comparatively numerous experimental and individual theoretical studies of the vibrational spectra of carbonates in which the patterns of their changes during the substitution of cations were established for certain types of structures. However, systematic theoretical studies from a unified standpoint, carried out for all types of carbonate structures and having a predictive power in early works, are absent. The aim of this work is to theoretically study the dependences of the characteristics of the infrared and Raman spectra of carbonates crystallizing in the structures of calcite, dolomite, and aragonite on the radii and masses of metal cations. The parameters of vibrational spectra of carbonates were calculated within the framework of a unified approach based on the known experimental data of crystal structure. Furthermore, the results of our calculations were compared with the available experimental and theoretical parameters of the infrared and Raman spectra of carbonates and, on this basis, the general regularities of changes in the vibrational spectra were determined upon substitution of metal cations. Then, the information can be used as an instrument in the analysis of vibrational spectra of new crystalline compounds and solid solutions. The calculated quantitative dependences can also be used in noncontact nondestructive diagnostics of carbonates by spectroscopic techniques.

2. Calculation Method

The research of the ordinary optical properties dependences of metal carbonates were carried out within *ab initio* principles using the Hartree–Fock theory (HF) methods and density functional theory, which are well combined in the CRYSTAL17 program code [74,75]. The hybrid functional B3LYP, which includes the 20% HF exchange with the Becke exchange functional [76] and the LYP correlation functional [77], was used. The basic functions were chosen in the form of a linear combination of localized atomic orbitals of the Gaussian type. We used full-electronic basis sets for carbon, oxygen, magnesium, and calcium atoms from [78] and the gaussian basis sets of double-zeta valence with polarization quality basis set for zinc and cadmium atoms [79,80]. We used pseudopotential basis sets from [81] for strontium and barium, those of [82] for manganese, and those of [83] for lead.

The reciprocal space was sampled using a Monkhorst–Pack [84] grid with 216 independent *k*-points in the irreducible Brillouin zone for trigonal crystals, and 64 points for orthorhombic crystals. The accuracy of the self-matching procedure was no less than 10^{-9} a.u. (1 a.u. = 27.21 eV). The vibrational frequencies of the lattice atoms were calculated using the FREQCALC procedure [85,86]. The phonon harmonic frequencies ω_P at the point Γ ($k = 0$, the center of the first Brillouin zone) were obtained from the diagonalization of the mass-weighted Hessian matrix of the second derivatives of energy with respect to atomic displacements u [87,88]:

$$W_{ai,bj}^{\Gamma} = \frac{H_{ai,bj}^0}{\sqrt{M_a M_b}}, H_{ai,bj}^0 = \left(\frac{\partial^2 E}{\partial u_{ai}^0 \partial u_{bj}^0} \right) \tag{1}$$

where atoms *a* and *b* with masses M_a and M_b are displaced in the unit cell (index 0) from equilibrium positions along the *i*- and *j*-Cartesian directions, respectively. The first order derivatives were calculated analytically, whereas the second order derivatives were obtained numerically. The intensity of IR absorption for the ν-vibration was calculated using the Born effective charge tensor Z^*, which characterizes the change in dynamics and the electronic configuration of atom

displacement. The relative intensities of the Raman peaks were calculated analytically using the extension scheme of the analytical calculation of IR intensity [89]. The proposed technique was previously used to study the ordinary properties of sulfates [90].

3. Crystal Structure

The crystal structure parameters of calcite, dolomite, norsethite, and aragonite types calculated in this work are shown in Table 1. There is a close agreement between the optimized and experimental parameters of the crystal lattice. Thus, the standard deviation $\Delta = \sqrt{\frac{1}{N}\sum_{i=1}^{N}\left(\frac{exp_i - theor_i}{exp_i}\right)^2}$ for $N = 5$ theoretical values from Table 1 and the experimental (exp) value for synthetic magnesite [30] is 1.6%, for natural calcite [29]—1.9%, for smithsonite [32]—1.5%, for synthetic otavite [36]—2.4%, for dolomite [38]—1.5%, and for norsethite [46]—3.6%. For four crystals with aragonite structure, the deviation of three lattice constants and two interatomic distances from experimental data for natural minerals [48] is 2.7%.

Table 1. Calculated lattice constants a, b, c, unit cell volume V, and average distances between the atoms of metal M and oxygen O (R_{M-O}) and carbon C and oxygen (R_{C-O}).

Carbonate	a, Å	b, Å	c, Å	V, Å³	R_{M-O}, Å	R_{C-O}, Å
$MgCO_3$	4.6624	4.6624	15.1891	285.9527	2.1229	1.2857
$CaCO_3$_C	5.0385	5.0385	17.3168	380.7118	2.3905	1.2878
$ZnCO_3$	4.7094	4.7094	15.1297	290.5952	2.1344	1.2973
$CdCO_3$	4.9819	4.9819	16.6163	357.1529	2.3312	1.2874
$CaMg(CO_3)_2$	4.8382	4.8382	16.2563	329.5605	2.2571	1.2865
$CdMg(CO_3)_2$	4.8140	4.8140	15.8629	318.3695	2.2253	1.2862
$CaMn(CO_3)_2$	4.8295	4.8295	15.8159	319.4686	2.2302	1.2874
$CaZn(CO_3)_2$	4.8558	4.8558	16.2964	332.7782	2.2648	1.2866
$BaMg(CO_3)_2$	5.0637	5.0637	17.0662	378.9683	2.6811	1.2846
$CaCO_3$_A	5.0020	8.0175	5.8581	234.9323	2.5604	1.2857
$SrCO_3$	5.1469	8.4418	6.1947	269.1522	2.6838	1.2884
$BaCO_3$	5.3665	8.9327	6.6847	320.4459	2.8567	1.2910
$PbCO_3$	5.2453	8.5723	6.3725	286.5319	2.7451	1.2897

As the physical quantities to describe the regularities of changes in the vibrational properties of carbonates from cationic substitution in the lattice, we used the mass of metal atoms (a.m.u.; Mg—23.985, Ca—39.963, Mn—54.938, Zn—63.929, Sr—87.906, Cd—113.904, Ba—137.905, and Pb—207.977) and the effective Shannon ionic radii [91]. The cationic radii of metals are determined by their electronic structure and depend on the coordination environment. The last filled electron shell of the magnesium ion is $2p^6$, and the radius of Mg^{2+} surrounded by six nearest neighbors is 0.72 Å. Similarly, for calcium: $3p^6$, 1.00 Å. In zinc and cadmium, the filled shells are $3d^{10}$ and $4d^{10}$, and the radii are 0.74 and 0.95 Å, respectively. In aragonite, each Ca^{2+} ion is already surrounded by nine oxygen atoms and, therefore, its effective radius is 1.18 Å. In the case of strontium and barium, the radii for the 9-fold environment are 1.31 and 1.47 Å, and for 12—1.44, 1.61 Å. The electronic configuration of lead [Xe] $4f^{14}5d^{10}6s^26p^2$ distinguishes it from other elements; therefore, the radius of 9-coordinated Pb^{2+} is 1.35 Å, which is larger than that of strontium, but smaller than that of barium. Transition metals have partially filled $3d$ shells with the number of electrons from 5 to 8, and decreasing radii for Mn^{2+} (0.83 Å), Fe^{2+} (0.78 Å), and Co^{2+} (0.745 Å). Following [33], we write the chemical formula of an arbitrary solid solution as $M1_{X1}M2_{X2}M3_{X3}CO_3$, $X1 + X2 + X3 = 1$. Then, the average radius of the cation is determined as $<R_M> = X1 \cdot R_{M1} + X2 \cdot R_{M2} + X3 \cdot R_{M3}$, where R_{M1}, R_{M2}, R_{M3} are radii of divalent ions $M1^{2+}$, $M2^{2+}$, $M3^{2+}$. For dolomite, the cation radius is 0.86 Å, and for norsethite—1.165 Å. The average atomic mass of metals is calculated in a similar way.

It is convenient to describe the change in crystal cell parameters or frequencies (intensities) of the vibrational spectra y on the radii of cations or their masses (r) using the linear dependence $y(r) =$

$y_0 + y_1 \cdot r$, where y_0 is the value of the function at $r = 0$, y_1—derivative of the function y, characterizing the rate of change of the corresponding value. The obtained calculated data $y(r_i)$, $I = 1, N$ are approximated by a linear dependence (fit), and the accuracy of this procedure is controlled by the relation: $K = \sqrt{\sum_{i=1}^{N} \left(y_i^{fit} - \overline{y^{fit}}\right)^2 / \sum_{i=1}^{N} \left(y_i^{data} - \overline{y^{data}}\right)^2}$, where the average value $\overline{y} = \frac{1}{N}\sum_{i=1}^{N} y_i$.

The change in the calculated unit cell volume of carbonates by one formula unit V/Z from the cation radii R_M obeys the linear dependence $V/Z(\text{Å}^3) = 25.22 + 31.54 \cdot R_M$ with a correlation coefficient of 0.936. The large slope of this dependence of 31.54 Å^2 indicates that the replacement of the cation is of great importance for carbonates. The indicated dependence with the experimental values of volumes has the form $V/Z(\text{Å}^3) = 22.48 + 36.2482 \cdot R_M$ (Å^3) with the coefficient $K = 0.945$. For each individual lattice type, the correlation coefficient is much better: for calcite and aragonite, 0.995, and for dolomite, 0.969. The linear dependence is explained by the fact that the cell volume is weakly related to the structure symmetry but is determined by the stacking of layers of polyhedrons, which depends on the ionic radii of the substitutional atoms. According to Vegard's law, the unit cell parameters change linearly depending on the composition, and for trigonal crystals, it can be written as: $a(\text{Å}) = 4.008 + 0.959 \cdot R_M$ (0.941), $c(\text{Å}) = 11.772 + 4.917 \cdot R_M$ (0.88). Hereinafter, the coefficient K is indicated in brackets. The linear dependence for all carbonates is fulfilled for the average distance between metal M and oxygen O: $R_{M-O}(\text{Å}) = 1.374 + 1.02 \cdot R_M$ (0.985) with high accuracy.

4. Vibrational Spectra

The rhombohedral cell of calcite contains ten atoms, and 30 possible vibrational modes can be classified for it, according to irreducible representations of the point group as: $\Gamma_{tot} = A_{1g}(R) + 3A_{1u} + 3A_{2g} + 3A_{2u}(IR) + 4E_g(R) + 6E_u(IR)$. A_{1g} and $4E_g$ modes are active in Raman spectra (R), $3A_{2u}$ and $5E_u$ modes are active in infrared (IR), A_{1u} and $3A_{2g}$ modes are spectroscopically inactive, and $1A_{2u}$ and $1E_u$ modes are acoustic. Nine translational modes will refer to the symmetry $A_{2g} + A_{1u} + A_{2u} + E_g + 2E_u$, six librational modes to $A_{2g} + A_{2u} + E_g + E_u$, and twelve internal vibrations to $A_{1g} + A_{2g} + A_{1u} + A_{2u} + 2E_g + 2E_u$. Modes of the A_{2u} symmetry have polarization $E||z$ and modes of E_u symmetry have $E \perp z$ polarization. Internal vibrations of E_u symmetry are of the ν_4 type (in-plane bending), A_{2u} modes are of the ν_2 type (out-of plane bending), and E_u symmetry are of the ν_3 type of symmetric stretching. In the Raman spectrum, the ν_4 (in-plane asymmetric stretching) mode has E_g symmetry, the ν_1 symmetric stretch mode has A_{1g} symmetry, and a ν_3 asymmetric stretch type has E_g symmetry.

For dolomite structure, the expansion of the vibrational representation according to irreducible representations is $\Gamma_{tot} = 4A_g(R) + 6A_u(IR) + 4E_g(R) + 6E_u(IR)$. Nine translational modes refer to symmetry $A_g + 2A_u + E_g + 2E_u$, six rotational modes refer to $A_g + A_u + E_g + E_u$, and 12 internal modes refer to $2A_g + 2A_u + 2E_g + 2E_u$. For the norsethite type structure with the space group $R-3m$, the expansion of the vibrational representation is: $\Gamma_{tot} = 3A_{1g}(R) + 2A_{1u} + A_{2g} + 5A_{2u}(IR) + 4E_g(R) + 6E_u(IR)$. For the aragonite orthorhombic structure, the symmetry of the carbonate group decreases to C_s. There will be 60 vibrational modes in total, where $1B_{1u} + 1B_{2u} + 1B_{3u}$ are acoustic. The vibrational representation is decomposed into irreducible representations as $\Gamma_{tot} = 9A_g + 6B_{1g}(R) + 9B_{2g}(R) + 6B_{3g}(R) + 6A_u + 9B_{1u}(IR) + 6B_{2u}(IR) + 9B_{3u}(IR)$. The B_{2u} symmetry modes have polarizations $E||x(a)$, B_{3u}—$E||y(b)$, B_{1u}—$E||z(c)$. There will be 24 internal modes, eight of the ν_4 and ν_3 types, and four of the ν_2 and ν_1 types. The available experimental and theoretical data on vibration spectra of the carbonates under consideration are summarized in Supplementary Materials [92–110].

5. Optical Spectra of Crystals with a Calcite Structure

The infrared absorption spectra (IRS) and Raman scattering spectra (RS) of calcite-structured carbonates calculated in this work, obtained by Gaussian broadening of normal long-wavelength vibrations, are shown in Figure 2. The obtained wavenumbers of vibrations active in the IRS of calcites, together with the available experimental data, are given in Table S1; for the vibrations active in RS, they are given in Table S2 in the Supplementary materials. A good agreement was observed between the calculated vibration wavenumbers and the experimentally measured values. Thus, the average root-square deviations for eight IRS-active wavenumbers obtained by the B3LYP method for

magnesite and determined experimentally in [92] and [58] do not exceed 4.0% and 3.3%, respectively. There is also a good agreement with the calculated data of the authors of [93] (4.7%) and [94] (3.5%). The root-mean-square deviations for the wavenumbers of five vibrations active in RS, obtained by the B3LYP method in this work, are 1.3% (1.0%) in the experiment in [95] for magnesite (calcite), 1.5% (1.4%) for the experiment in [58], 1.6% (1.1%) for the experiment in [61], and 1.6% (1.7%) for the experiment in [73]. For four studied carbonates with five vibrations active in RS, in a matrix of 20 values, the deviation of the B3LYP calculation results from the experimental values [64] is 2.4%.
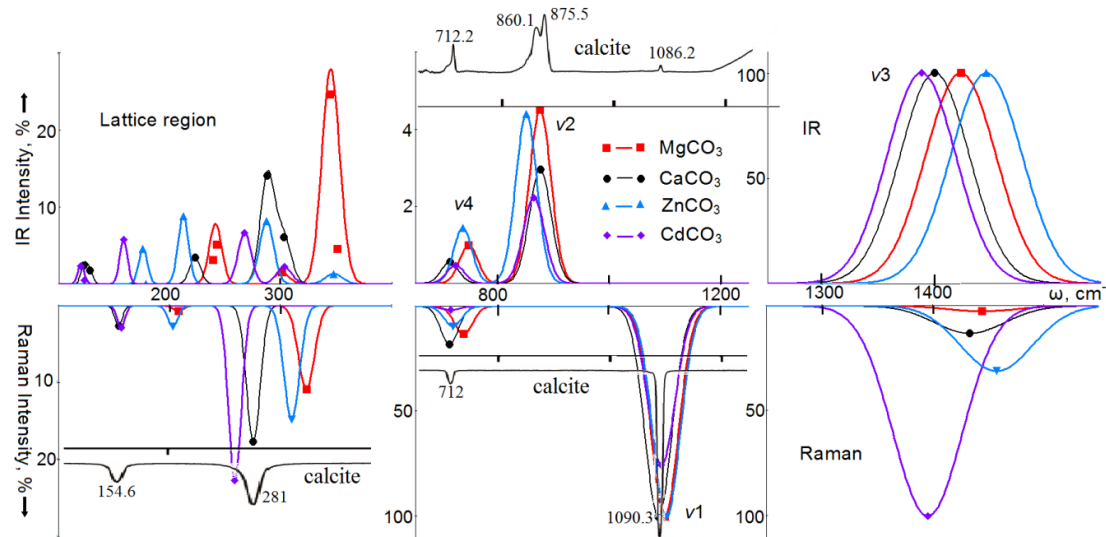

Figure 2. Calculated infrared spectra (IR) (top) and spectra of Raman light scattering (bottom) of intramolecular ν1, ν2, ν3, ν4, and lattice vibrations of magnesium (red, squares), calcium (black, circles), zinc (blue, triangles), and cadmium (lilac, rhombuses) carbonates with a calcite structure. For comparison, the experimental spectra of calcite are given [68].

In $MgCO_3$, the most intense mode (5132 km/mol) in IRS corresponds to the internal vibration ν3 of E_u symmetry with the wavenumber of 1424 cm⁻¹. Taking its intensity as 100%, for the ν2 vibration with a wavenumber of 874 cm⁻¹, we obtained 4%, and for the ν4 (746 cm⁻¹) mode, even less—0.9%. In calcite, the wavenumbers corresponding to the vibrations ν3, ν2, and ν4 are 1400, 875, and 712 cm⁻¹, and their intensities are 5447 km/mol (100%), 3%, and 0.5%, which practically do not differ from magnesite. For $ZnCO_3$ and $CdCO_3$, the structures of the spectra in the high-frequency region remain similar to magnesite. Thus, for internal modes, there is a linear correlation between the change in the wavenumber and the radius of the cation R_M. For ν4, it can be written in the form: $\omega_{Eu}(cm^{-1}) = 812.9 - 98.7 \cdot R_M$ (0.958), and with a smaller K coefficient for ν3: $\omega_{Eu}(cm^{-1}) = 1546.9 - 154.8 \cdot R_M$ (0.854). A good correlation ($K = 0.96$) for the calculated intensity is observed for the ν3 vibrations, where it increases with rise of atomic mass as: $I(km/mol) = 4948 + 14 M$, and, for the ν2 mode, it decreases with increasing radius: $I(km/mol) = 478 - 326 R_M$.

For lattice vibrations of $MgCO_3$, the most intense ones are the E_u symmetry modes with wavenumbers of 344 cm⁻¹ (25%), 301 cm⁻¹ (2%), and A_{2u} symmetry modes at 351 cm⁻¹ (4%), 242 cm⁻¹ (5%). For $CaCO_3$, the lattice modes are shifted to the low-wavenumber region, and their intensities decrease. In the region of lattice vibrations of $ZnCO_3$, the most intense modes will be E_u symmetry with wavenumbers of 287 cm⁻¹, 212 cm⁻¹, and only then with A_{2u} symmetry: 348 cm⁻¹, 176 cm⁻¹. In $CdCO_3$, this trend continues. Thus, for translation modes of E_u symmetry, a dependence on the cation mass is observed: $\omega(cm^{-1}) = 306.0 - 1.37 \cdot M$ (0.915). For the rest of the lattice modes, the best linear dependence was established for the cation radius: for rotational ones: $\omega_{Eu}(cm^{-1}) = 466.5 - 353.1 \cdot R_M$ (0.91), $\omega_{A2u}(cm^{-1}) = 463.2 - 348.5 \cdot R_M$ (0.884, and for translational modes: $\omega_{A2u}(cm^{-1}) = 484.7 - 186.3 \cdot R_M$ (0.991).

In RS, the intense line (taken as 100%) in Figure 2 is due to vibrations of the ν_1 type, and falls on 1099 cm^{-1} in MgCO$_3$, and 1087 cm^{-1} in calcite. This mode has a significant polarization dependence [89]: the *xx* and *yy* components are ten times larger than the *zz* component. Internal vibrations of ν_4 type also have a noticeable intensity: for magnesite—with a wavenumber of 737 cm^{-1}, for calcite—711 cm^{-1}, and also for ν_3 type: 1444 cm^{-1} and 1433 cm^{-1}, respectively. In carbonates of relatively heavy metals zinc and cadmium, the positions of the maxima of the ν_4 and ν_1 bands are practically preserved (ω_{Eg}(cm^{-1}) = 783.3 − 72.9·R_M (0.906), ω_{A1g}(cm^{-1}) = 1138.0 − 49.2·R_M (0.906)), whereas for the ν_3 region the changes are significant. This is due to the fact that the intensity of this mode increases linearly with an increase in the atomic mass of the metal cation: $I_{\nu3}$(%) = −29.9 + 1.1·M (0.987). For CdCO$_3$, the ν_3 vibration becomes the most intense in RS and has pronounced *xz* and *yz* polarizations.

For lattice vibrations, the most intense vibration in the RS spectrum has the E_g symmetry, and its wavenumbers in MgCO$_3$ are 323 cm^{-1} (intensity 11%), ZnCO$_3$ 310 cm^{-1} (15%), CdCO$_3$ 258 cm^{-1} (23%), and CaCO$_3$ 275 cm^{-1} (18%). Thus, for the lattice translational vibration, there is a linear dependence of the form ω(cm^{-1}) = 361.0 − 210.6·R_M (0.992), and for rotational, ω(cm^{-1}) = 449.0 − 185.5·R_M (0.912). Since there is a good linear relationship between $R_{M–O}$ and the radius of the R_M cation, the above formulas can easily be rewritten for distances as well. The above formulas allow predicting the wavenumber values for other carbonates; thus, for the lattice modes E_g(T), E_g(L), internal ν_4 and ν_1, the wavenumbers predicted by the formulas for MnCO$_3$ are 186, 296, 723, and 1097 cm^{-1}, and for CoCO$_3$, they are 204, 311, 729, and 1101 cm^{-1}. The experimental values for rhodochrosite are 184, 290, 719, and 1086 cm^{-1} [62]; for spherocobaltite, they are 194, 302, 725, and 1090 cm^{-1} [34].

6. Vibrational Spectra of Crystals with a Dolomite Structure

The IRS and RS of carbonates with the dolomite structure are given in Figure 3, and Tables S3 and S4 of the accompanying materials show the wavenumbers of normal long-wave vibrations of crystals with the dolomite and norsethite structures, calculated by the B3LYP method and measured experimentally. The examination of these tables shows that there is a satisfactory agreement between the wavenumbers of lattice [69] and internal [61] vibrations of natural dolomite calculated and measured in IRS. The root-mean-square deviation is 8.7 and 1.0%, respectively. For the wavenumbers of vibrations active in RS, the root-mean-square deviation of the results of this calculation from the experimental values is 1.4%. In crystals with a dolomite structure, the picture of theoretical spectra does not differ significantly from the calcite spectra. In IRS CaMg(CO$_3$)$_2$, the most intense mode (5318 km/mol, 100%) is the ν_3 mode at 1416 cm^{-1}. The internal vibration ν_2 with a wavenumber of 877 cm^{-1} has an intensity of 3.5%, and for vibration ν_4 at 727 cm^{-1}, the intensity is close to 1%. Unlike calcite, the vibration ν_1 of the A_u symmetry is allowed by symmetry; however, its intensity is practically zero. The most intense (19%) in the region of lattice vibrations is the E_u symmetry mode with a wavenumber of 337 cm^{-1}. Modes of the same symmetry, but with a much lower intensity, appear at 257 (2.5%) and 167 cm^{-1} (4%).

In CdMg(CO$_3$)$_2$, the most intense (5788 km/mol, 100%) vibration will be ν_3 with a wavenumber of 1407 cm^{-1}, and for lattice vibration with a wavenumber of 338 cm^{-1}, the intensity is 16%. A similar picture is observed in CaZn(CO$_3$)$_2$, where the intensity of the ν_3 vibration is 5928 km/mol (100%), and the intensities of two lattice vibrations with wavenumbers of 290 and 310 cm^{-1} are 11% and 3.5%, respectively. The situation is different in CaMn(CO$_3$)$_2$, where the intensity of the ν_3 mode is much lower—1121 km/mol (100%), and against its background, the relative intensities of other ν_2 and ν_4 vibrations increased to 22 and 6%, respectively.

The RS of dolomite will be dominated by a fully ν_1 symmetric vibration with a wavenumber of 1097 cm^{-1}. Its full intensity is taken as 100%. Then, the intensities of the ν_4, ν_2, and ν_3 modes will be 15%, 0.2% and 9%, respectively. In the region of lattice vibrations, the most intense are the E_g symmetry modes with wavenumbers of 296 cm^{-1} (13%) and 175 cm^{-1} (3%). In CdMg(CO$_3$)$_2$, the ν_1 mode does not change in wavenumber and remains most intense. The wavenumber of the ν_3 mode decreases, but its intensity sharply increases to 49%. In CaMn(CO$_3$)$_2$, the intensity of the ν_3 mode becomes maximum (taken as 100%), while for the ν_1 vibration it is only 15%. Thus, as for IRS, the

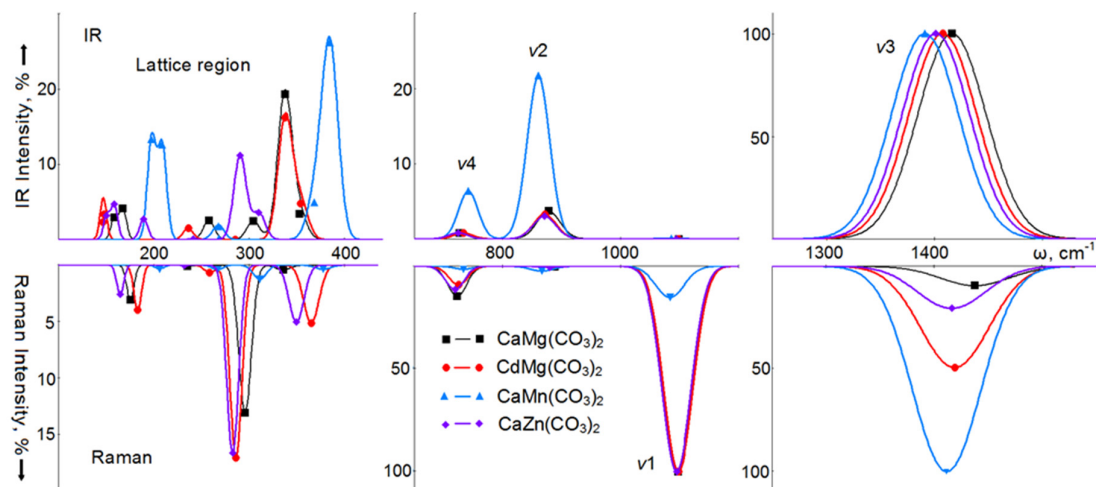binary carbonate $CaMn(CO_3)_2$ differs from other crystalline dolomites in the parameters of its vibrational spectra.

Figure 3. Calculated infrared spectra (IR) (top) and Raman spectra (bottom) of intramolecular $\nu 1$, $\nu 2$, $\nu 3$, $\nu 4$, and lattice vibrations of double calcium-magnesium (black, squares), cadmium-magnesium (red, circles), calcium-manganese (blue, triangles), and calcium-zinc carbonates (lilac, rhombuses) with a dolomite structure.

In IRS of the $BaMg(CO_3)_2$ crystal (Figure 4) in the region of intramolecular vibrations, the most intense (5194 km/mol) vibration will be $\nu 3$ with a wavenumber of 1439 cm^{-1}. Against this background, the $\nu 2$ vibration with a wavenumber of 878 cm^{-1} and the intensity of 3% is almost imperceptible, moreover, the $\nu 4$ vibrations (694 cm^{-1}, 0.5%) and $\nu 1$ allowed here (1125 cm^{-1}, 0.2%) practically do not appear. In the region of lattice vibrations, vibrations of E_u symmetry with wavenumbers of 315, 200, and 106 cm^{-1} stand out in intensity, while less intense vibrations of A_{2u} symmetry have wavenumbers of 347 and 115 cm^{-1}. The first of these less intense vibrations corresponds to the displacements of magnesium atoms in antiphase with the anions, and the second corresponds to the displacements of barium atoms. Magnesium atoms are also involved in the formation of this mode, and they shift synchronously with the anion. In RS of $BaMg(CO_3)_2$, vibrations of anion atoms will also dominate: $\nu 1$ with a wavenumber of 1126 cm^{-1} (its intensity is taken as 100%), $\nu 2$ of the same symmetry and intensity of 3%, as well as doubly degenerated $\nu 4$ (697 cm^{-1}) and $\nu 3$ (1444 cm^{-1}) with intensities of 21% and 3%, respectively. For lattice vibrations, the A_{1g} symmetry mode with a wavenumber of 284 cm^{-1} and E_g symmetry modes with wavenumbers of 108 and 254 cm^{-1} will be noticeable, of which the first is rotational, and the second is translational vibration.

Let us establish ordinary dependences for the entire class of trigonal crystals. For the lowest-wavenumber lattice translational vibration in IRS $\omega_{Eu}(cm^{-1}) = 379.0 - 244.3 \cdot R_M$ (0.794); for RS, $\omega_{Eg}(cm^{-1}) = 367.3 - 216.2 \cdot R_M$ (0.896), and $\omega_{Eg}(cm^{-1}) = 413.1 - 39.6 \cdot R_M$ (0.813). Using the first formula, we obtain for ankerite $(CaFe(CO_3)_2)$ 164 cm^{-1} (in experiment, 166 cm^{-1} [72]), kutnogorite $Ca_{0.78}Mn_{1.13}(CO_3)_2$ 159 cm^{-1} (153 cm^{-1}). For lattice vibrations active in RS, the formulas give estimated values for rhodochrosite $(MnCO_3)$ 188, 297 cm^{-1}. The experimental values are 185 and 290 cm^{-1} [73].
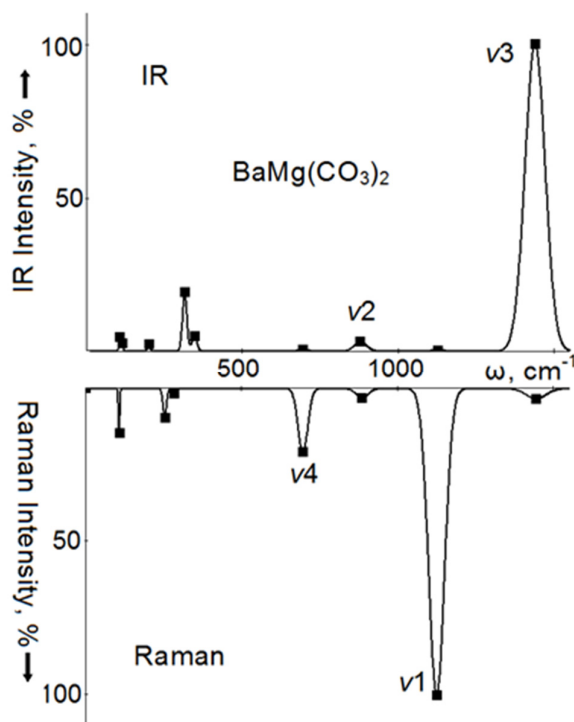
Figure 4. Calculated infrared spectrum (IR) (top) and Raman spectrum (bottom) of intramolecular ν1, ν2, ν3, ν4, and lattice vibrations of double barium-magnesium carbonate in a norsesite-type structure. The solid line is the Gaussian broadening of the frequencies of long-wave oscillations (squares).

7. Vibrational Spectra of Crystals with Aragonite Structure

The calculated spectra of infrared absorption and Raman light scattering of calcium, strontium, lead, and barium carbonates with aragonite structure are shown in Figure 5. The wavenumbers of normal long-wave vibrations of crystals with the aragonite structure calculated by the B3LYP method, together with the available experimental and theoretical data, are summarized in Tables S5–S8 of the Supplementary Materials. The comparison of wavenumbers calculated by the B3LYP method with the experimental values shows that the root-mean-square deviation for four ν1–ν4 wavenumbers in four carbonates is, according to [68], 1.5% for IRS; 0.8% for RS; for IRS [55]—2.0%, and for RS [57]—0.9%.

In the IRS of aragonite, the most intense vibrations are of the ν3 type with the B_{2u}, B_{3u} symmetry, wavenumbers of 1448 and 1480 cm^{-1} and intensities of 4523 and 4727 km/mol. In Figure 4, they correspond to a broad intense band with the maximum at 1462 cm^{-1} (1461 cm^{-1} in [68]). For convenience of comparison, the intensity of vibration of B_{3u} symmetry is taken as 100%. In SrCO$_3$, the maximum intensity of the B_{3u} mode at 4757 km/mol is taken as 100%, in BaCO$_3$, the B_{2u} symmetry modes at 4953 km/mol, and in PbCO$_3$: 6241 km/mol. Thus, the intensity ν3 increases with the atomic mass of the metal, and the position of the maximum in the series changes according to the law: $\omega(cm^{-1}) = 1480.2 - 0.365 \cdot M$ (cm^{-1}) with a correlation coefficient of 0.991.

Unlike calcite, in the infrared spectra of aragonite, the vibration of the ν1 type will be active due to the modes of symmetry B_{3u}, B_{1u}. In the spectrum shown in Figure 4, they correspond to a weak (0.2%) band with a maximum at 1090 cm^{-1}, the wavenumber of which shifts towards lower values with increasing atomic mass: $\omega(cm^{-1}) = 1090.6 - 0.127 \cdot M$. The intensity of vibrations of the ν2 type of B_{1u} symmetry is much higher than that of ν1 vibrations, it decreases with an increase in the atomic mass of the metal, and its wavenumber practically does not change: $\omega(cm^{-1}) = 893.3 - 0.065 \cdot M$. In the experimental spectra, this dependence has the form: $\omega(cm^{-1}) = 866.2 - 0.123 \cdot M$. Vibrations of the ν4 type in CaCO$_3$ and SrCO$_3$ correspond to the modes of symmetries B_{3u}, B_{2u} with distances between wavenumbers of 13 and 6 cm^{-1}. In BaCO$_3$ and PbCO$_3$, the distances between wavenumbers decrease

to 2 and 3 cm^{-1}. This behavior of vibrational modes of the v_4 type is consistent with experimental data [68], where it was found that two peaks are observed in aragonite (CaCO$_3$) and strontianite (SrCO$_3$), and only one for cerussite (PbCO$_3$) and witherite (BaCO$_3$). There is a good ordinary dependence of the peak position on the atomic mass of the metal: in the experiment it is $\omega(cm^{-1}) = 707.5 - 0.128 \cdot M$, and in the calculation: $\omega(cm^{-1}) = 715.4 - 0.119 \cdot M$, with the correlation coefficients 0.944 and 0.977, respectively.
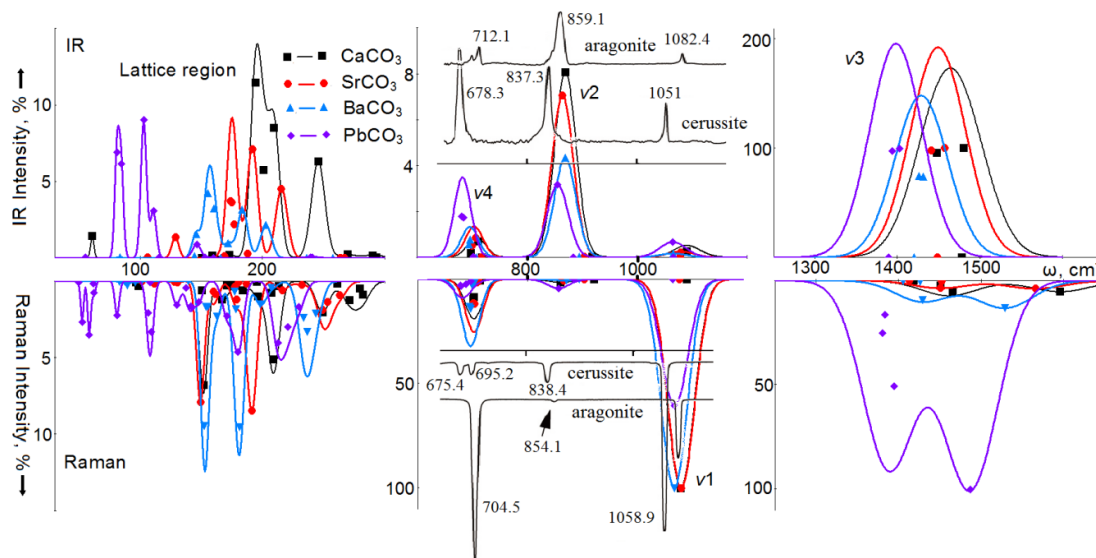

Figure 5. Calculated infrared spectra (IR) (top) and Raman spectra (bottom) of intramolecular v_1, v_2, v_3, v_4, and lattice vibrations of calcium (black, squares), strontium (red, circles), barium (blue, triangles), lead carbonates (lilac, rhombuses) with aragonite structure. For comparison, the experimental spectra of aragonite and cerussite are given [68] (Reproduced with permission from [68]; Copyright Springer Nature, 2020).

In the Raman spectrum of aragonite (CaCO$_3$), v_1 vibration of A_g symmetry with a wavenumber of 1078 cm^{-1} is the most intense (taken as 100%). Vibrations v_4 of the A_g and B_{1g} symmetries with intensities of 9% each are also noticeable, which form the maximum in the spectrum shown in Figure 5 at 702 cm^{-1}. In BaCO$_3$, the v_1 vibration maximum shifts to 696 cm^{-1}, and its intensity increases. In addition, the width of this peak increases. Oscillations of the v_3 type in CaCO$_3$ have B_{3g} (1465 cm^{-1}) and B_{2g} (1595 cm^{-1}) symmetries, and an intensity of 5%. In SrCO$_3$, these are vibrations at wavenumbers of 1450 and 1565 cm^{-1} with intensities of 4%. In BaCO$_3$, they shift to lower values of 1429 and 1528 cm^{-1}, and the intensities increase to 9 and 13%. Oscillations of the B_{2g} symmetry correspond to the displacements of atoms to the C–O bonds along the *b* axis, whereas B_{3g}—along the *a* axis, perpendicular to the layers of anions and cations.

The Raman spectrum of PbCO$_3$ differs from the spectra of other carbonates with the aragonite structure. Here, the most intense (taken as 100%) is the vibration of the v_3 type of B_{2g} symmetry with a wavenumber of 1486 cm^{-1} [68]. Three other vibrations of this type have B_{3g}, A_g, B_{1g} symmetries, similar wavenumbers of 1394, 1383 and 1380 cm^{-1} and intensities of 50%, 16%, and 25%, respectively. They form a second maximum in RS at 1388 cm^{-1}. The v_1-type vibration with a wavenumber of 1067 cm^{-1} has an intensity of 61%. Modes of the same A_g symmetry are also dominant in the formation of the v_2 band, the position of which in aragonites obeys the law: $\omega(cm^{-1}) = 895.6 - 0.117 \cdot M$ with a high correlation coefficient of 0.977.

In the IRS of aragonite, in the region of lattice vibrations, there is a maximum at 245 cm^{-1}, formed by the B_{3u} symmetry mode with an intensity of 13%, and the main maximum with an intensity of 23% at 194 cm^{-1} (B_{2u} symmetry). For SrCO$_3$, four peaks are observed at 129, 175, 192 and 215 cm^{-1} with intensities of 3, 18, 15 and 9%, while in BaCO$_3$ the intense band is at 157 cm^{-1} (B_{1u} and B_{3u}) with a low-wavenumber band at 146 cm^{-1}, and high-wavenumber at 171 cm^{-1} shoulders. In PbCO$_3$, the main

features of the spectrum are shifted to the low-wavenumber region. There are two main peaks at 82 cm^{-1} with an intensity of 17%, and a peak at 103 cm^{-1} and an intensity of 18%. This structure of the IRS in the lattice region is consistent with the results of measurements [72], where it was found that the broad band at 263 cm^{-1} in the structure of aragonite shifts to longer wavelengths with an increase in the atomic number of the metal: up to 227 cm^{-1} in strontianite, then up to 205 cm^{-1} in witherite, and, finally, up to 136 cm^{-1} in cerussite.

For lattice vibrations of aragonite in RS, there will be three main bands with maxima at 152 cm^{-1}, 209 cm^{-1} and 250, 276 cm^{-1}. There is a good agreement between the calculated and experimental data [68]. In SrCO$_3$, there are two intense bands with maxima at 150 and 191 cm^{-1}, formed by the modes of symmetries B_{3g}, B_{2g}, and a weak band at 252 cm^{-1}. In the BaCO$_3$ spectrum, the maximum of the first band is at 153 cm^{-1}, the second at 181 cm^{-1} with a shoulder at 198 cm^{-1}, and the third at 237 cm^{-1}. The second maximum is formed by modes with B_{2g} symmetry with pronounced yz polarization. The spectrum of PbCO$_3$ contains a large number of bands of low intensity, not exceeding 6%.

In [68], it was found that RS and IRS confirm the general trend that each of the internal modes is shifted to lower wavenumbers in the following order: aragonite → strontianite → witherite → cerussite. The coefficients of linear interpolation of the wavenumbers of intramolecular (ν_4, ν_1, ν_3) vibrations active in RS for carbonates with the aragonite structure, obtained from experimental data [68] and theoretical calculations using the B3LYP method are summarized in Table 2. In the calculations, each type of vibration was determined as the average of the individual modes, which are shown in Table S9. For lattice vibrations, similar linear dependences are also obtained, as recorded in Table S10.

Table 2. Linear interpolation coefficients of the wavenumbers of intramolecular (ν_4, ν_1, ν_3) vibrations of the M cation mass for carbonates with aragonite structure, active in RS, obtained from experimental data [68] and theoretical calculations by the B3LYP method. The correlation coefficient is shown in brackets.

Method	ν_4	ν_1	ν_3	ν_3
Experiment [68]	713.2 − 0.173·M (0.986)	1090.1 − 0.17·M (0.919)	1495.3 − 0.588·M (0.989)	1597.2 − 0.582·M (0.99)
B3LYP	714.3 − 0.128·M (0.933)	1087.059 − 0.116·M (0.894)	1486.0 − 0.426·M (0.992)	1619.0 − 0.638·M (0.998)

As a check of the obtained formulas, we will use the available data [49], where the Raman spectra of (CaCO$_3$) X1 (SrCO$_3$) X2 (BaCO$_3$) X3 solid solutions were measured. Thus, in the spectrum of the composition 0.34:0.33:0.33, wavenumbers of 1452, 1086, 711, 273, 192, 155 cm^{-1} were observed. Calculation according to the formulas of Tables S8 and S9 gives: 1466, 1077, 703, 262, 183, and 158 cm^{-1}, that is, the root mean square deviation of the calculated and experimentally determined wavenumbers is about 2.7%.

8. Conclusions

In this work, the Hartree–Fock theory and the electron density functional in the form of a hybrid B3LYP functional in the basis of a linear combination of atomic orbitals by means of the CRYSTAL17 program code are used to calculate the structure and normal long-wavelength vibrations of MgCO$_3$, CaCO$_3$, ZnCO$_3$, CdCO$_3$ in the structure of calcite, CaMg(CO$_3$)$_2$, CdMg(CO$_3$)$_2$, CaMn(CO$_3$)$_2$, CaZn(CO$_3$)$_2$—in the structure of dolomite, BaMg(CO$_3$)$_2$—in the structure of the norsethite type, CaCO$_3$, SrCO$_3$, BaCO$_3$, PbCO$_3$—in the structure of aragonite. The analysis of the calculated results and their comparison with the available experimental data shows that the wavenumbers and intensities of individual vibrational modes obey the ordinary laws. For the calcite family, the intramolecular modes of the ν_2 and ν_3 types that are active in IRS correlate with the cation radius $\omega(\text{cm}^{-1}) = 812.9 - 98.7 \cdot R_M$, and $\omega(\text{cm}^{-1}) = 1546.9 - 154.8 \cdot R_M$ with correlation coefficients of 0.958 and 0.854. Vibration of the ν_4 type is active in RS, where the dependence of its wavenumber on the radius of the metal cation has the form $\omega(\text{cm}^{-1}) = 783.3 - 72.9 \cdot R_M$, and for the most intense ν_1: $\omega(\text{cm}^{-1}) = 1138.0 - 42.9 \cdot R_M$, with coefficients of correlation 0.906. For the entire class of trigonal crystals (calcite, dolomite, norsethite), the dependence of low- wavenumber lattice vibrations has the form for E_u

symmetry: E_u: $\omega(cm^{-1}) = 379.0 - 243.3 \cdot R_M$, and E_g: $\omega(cm^{-1}) = 367.3 - 216.2 \cdot R_M$, $\omega(cm^{-1}) = 413.1 - 139.6 \cdot R_M$. For carbonates with aragonite structure for the calculated wavenumbers ν_4, ν_2, ν_1, ν_3, linear dependences with high correlation coefficients are obtained for the atomic mass: $\omega(cm^{-1}) = 714.3 - 0.128 \cdot M$; $\omega(cm^{-1}) = 895.6 - 0.117 \cdot M$; $\omega(cm^{-1}) = 1087.1 - 0.116 \cdot M$; $\omega(cm^{-1}) = 1619.0 - 0.638 \cdot M$, and for IRS: $\omega(cm^{-1}) = 715.4 - 0.119 \cdot M'$; $\omega(cm^{-1}) = 893.3 - 0.065 \cdot M$; $\omega(cm^{-1}) = 1090.6 - 0.127 \cdot M$; $\omega(cm^{-1}) = 1480.2 - 0.365 \cdot M$. For trigonal and orthorhombic carbonates, linear dependences of metal substitution were established for the radius of the RM cation (the distance between the metal and oxygen R_{M-O}) only for the infrared in-plane bending mode ν_4: $\omega(cm^{-1}) = 786.2 - 65.88 \cdot R_M$ ($\omega(cm^{-1}) = 881.0 - 67.13 \cdot R_{M-O}$), and Raman in-plane asymmetric stretching mode ν_4: $\omega(cm^{-1}) = 768.5 - 53.24 \cdot R_M$ ($\omega(cm^{-1}) = 844.2 - 53.83 \cdot R_{M-O}$), with a correlation coefficient of 0.87 (0.91). For the rest of the modes, it was not possible to obtain linear dependences with high correlation coefficients.

Thus, *ab initio* predictions, with a relatively low computational capacity, can reproduce the full vibrational spectra of crystalline compounds of material science interest, and, on the basis of ordinary spectral dependences, predict their features for solid crystalline solutions. The obtained quantitative dependences of the characteristics of vibrational modes can be used in non-contact non-destructive diagnostics of carbonates by optical methods.

Supplementary Materials: The following are available online at www.mdpi.com/2079-4991/10/11/2275/s1, Table S1: Wavenumbers (cm^{-1}) of lattice, translational (T), rotational (L) and internal mode vibrations active in IR spectra (IR), obtained in this work by the B3LYP method, measured experimentally (Exp.) and calculated (Theor.) for carbonates with calcite structure, Table S2: Wavenumbers (cm^{-1}) of lattice, translational (T), rotational (L), and internal modes vibrations active in the Raman spectra, obtained in this work by the B3LYP method, measured experimentally [Exp] and calculated [Theor] in the works of other authors for carbonates with calcite structure, Table S3: Wavenumbers (cm^{-1}) of lattice and internal modes vibrations active in the IR spectra, obtained in this work by the B3LYP method, measured experimentally [Exp.] and calculated [Theor.] in the works of other authors for carbonates with dolomite and norsethite structure, Table S4: Wavenumbers (cm^{-1}) of lattice and internal modes vibrations active in Raman spectra, obtained in this work by the B3LYP method, measured experimentally [Exp.] and calculated [Theor.] in the works of other authors for carbonates with dolomite and norsethite structure, Table S5: Wavenumbers (cm^{-1}) of internal modes ν_1, ν_2, ν_3, ν_4 vibrations active in infrared spectra (IRS) calculated by the B3LYP method, measured experimentally [Exp.] and calculated [Theor.] in the works of other authors for crystals with aragonite structure, Table S6: Wavenumbers (cm^{-1}) of internal modes ν_1, ν_2, ν_3, ν_4 vibrations active in the Raman spectra, calculated by the B3LYP method, measured experimentally [Exp.] and calculated [Theor.] in the works of other authors for crystals with aragonite structure, Table S7: Wavenumbers (cm^{-1}) of lattice vibrations, active in infrared (IR) spectra, calculated by the B3LYP method, measured experimentally [Exp.] and calculated [Theor.] in the works of other authors for crystals with aragonite structure, Table S8: Wavanumbers (cm^{-1}) of lattice vibrations active in the Raman spectra, calculated by the B3LYP method, experimentally measured [Exp.] and calculated [Theor.] in the works of other authors for crystals with aragonite structure, Table S9: Values of the coefficients ω_0 (cm^{-1}), ω_1 (cm^{-1}/a.m.u.) of linear interpolation of frequencies $\omega = \omega_0 + \omega_1 \cdot M$ (cm^{-1}) by the atomic mass of the metal M intramolecular (ν_4, ν_2, ν_1, ν_3) modes, active in the Raman and infrared spectra absorption (IR) of carbonates with aragonite structure, obtained from theoretical calculations by the B3LYP method. The correlation coefficient K is shown in parentheses. Table S10: Values of the coefficients ω_0 (cm^{-1}), ω_1 (cm^{-1}/a.m.u.) of linear interpolation of wavenumbers $\omega = \omega_0 + \omega_1 \cdot M$ (cm^{-1}) by the atomic mass of the metal M of lattice vibrations active in the Raman spectra of carbonates with aragonite structure obtained from theoretical calculations by the B3LYP method. The correlation coefficient *K* is shown in parentheses.

Author Contributions: Y.N.Z.: Conceptualization, data curation, paper writing; V.V.A.: Conceptualization, paper writing. Both authors have read and agreed to the published version of the manuscript. All authors have read and agreed to the published version of the manuscript.

Conflicts of Interest: The authors declare no conflict of interest.

References

1. Liu, Y.; Shen, Y.; Zhao, S.; Luo, J. Structure-property relationship in nonlinear optical materials with p-conjugated CO_3 triangles. *Coord. Chem. Rev.* **2020**, *407*, 213152.

2. Hazen, R.M.; Downs, R.T.; Jones, A.P.; Kah, L. Carbon Mineralogy and Crystal Chemistry. *Rev. Mineral. Geochem.* **2013**, *75*, 7–46, doi:10.2138/rmg.2013.75.2.

3. Miller, K.G.; Kominz, M.A.; Browning, J.V.; Wright, J.D.; Mountain, G.S.; Katz, M.E.; Sugarman, P.J.; Cramer, B.S.; Christie-Blick, N.; Pekar, S.F. The Phanerozoic Record of Global Sea-Level Change. *Science* **2005**, *310*, 1293–1298, doi:10.1126/science.1116412.

4. Dupraz, C.; Reid, R.P.; Braissant, O.; Decho, A.W.; Norman, R.S.; Visscher, P.T. Processes of carbonate precipitation in modern microbial mats. *Earth-Sci. Rev.* **2009**, *96*, 141–162, doi:10.1016/j.earscirev.2008.10.005.

5. Litasov, K.D.; Goncharov, A.F.; Hemley, R.J. Crossover from melting to dissociation of CO_2 under pressure: Implications for the lower mantle. *Earth Planet. Sci. Lett.* **2011**, *309*, 318–323, doi:10.1016/j.epsl.2011.07.006.

6. Litasov, K.D.; Shatskiy, A.; Ohtani, E.; Yaxley, G.M. Solidus of alkaline carbonatite in the deep mantie. *Geology* **2013**, *41*, 79–82.

7. Montañez, I.P.; McElwain, J.C.; Poulsen, C.J.; White, J.D.; DiMichele, W.A.; Wilson, J.P.; Griggs, G.; Hren, M.T. Climate, pCO_2 and terrestrial carbon cycle linkages during late Palaeozoic glacial–interglacial cycles. *Nat. Geosci.* **2016**, *9*, 824–828, doi:10.1038/ngeo2822.

8. Sieber, M.J.; Wilke, F.; Koch-Müller, M. Partition coefficients of trace elements between carbonates and melt and suprasolidus phase relation of Ca-Mg-carbonates at 6 GPa. *Am. Mineral.* **2020**, *105*, 922–931, doi:10.2138/am-2020-7098.

9. Xie, M.; Yang, L.; Ji, Y.; Wang, Z.; Ren, X.; Liu, Z.; Asiri, A.M.; Xiong, X.; Sun, X. An amorphous Co-carbonate-hydroxide nanowire array for efficient and durable oxygen evolution reaction in carbonate electrolytes. *Nanoscale* **2017**, *9*, 16612–16615, doi:10.1039/c7nr07269d.

10. Sobhani-Nasab, A.; Pourmohamadian, H.; Rahimi-Nasrabadi, M.; Sheikhzadeh, G.A.; Tabrizi, H.B. Evaluation of the thermal properties of $SrCO_3$-microencapsulated palmitic acid composites as thermal energy storage materials. *J. Therm. Anal. Calorim.* **2020**, *140*, 2123–2130, doi:10.1007/s10973-019-08996-x.

11. De Beauvoir, T.H.; Sangregorio, A.; Cornu, I.; Josse, M. Synthesis, sintering by Cool-SPS and characterization of $A_2Cu(CO_3)_2$ (A = K, Na): Evidence for multiferroic and magnetoelectric cupricarbonates. *Dalton Trans.* **2020**, *49*, 7820–7828, doi:10.1039/d0dt00814a.

12. Lee, J.; Ryu, K.H.; Ha, H.Y.; Jung, K.-D.; Lee, J.H. Techno-economic and environmental evaluation of nano calcium carbonate production utilizing the steel slag. *J. CO_2 Util.* **2020**, *37*, 113–121, doi:10.1016/j.jcou.2019.12.005.

13. Mazhar, S.F.B.; Meyer, H.J.; Samuels, T.; Sharonov, M.; Shi, L.; Alfano, R.R. Exploration of the competition between O- and E-wave induced stimulated Raman and supercontinuum in calcite under ultrafast laser excitation. *Appl. Opt.* **2020**, *59*, 5252–5257.

14. Karuppaiah, M.; Akilan, R.; Sakthivel, P.; Asaithambi, S.; Shankar, R.; Yuvakkumar, R.; Hayakawa, Y.; Ravi, G. Synthesis of self-assembled micro/nano structured manganese carbonate for high performance, long lifespan asymmetric supercapacitors and investigation of atomic-level intercalation properties of OH^- ions via first principle calculation. *J. Energy Storage* **2020**, *27*, 101138.

15. Assaedi, H.; Alomayri, T.; Kaze, C.R.; Jindal, B.B.; Subaer, S.; Shaikh, F.; Alraddadi, S. Characterization and properties of geopolymer nanocomposites with different contents of nano-$CaCO_3$. *Constr. Build. Mater.* **2020**, *252*, 119137, doi:10.1016/j.conbuildmat.2020.119137.

16. Atuchin, V.V.; Kesler, V.G.; Kokh, A.E.; Pokrovsky, L.D. X-ray photoelectron spectroscopy study of b-BaB_2O_4 optical surface. *Appl. Surf. Sci.* **2004**, *223*, 352–360.

17. Ramana, C.V.; Vemuri, R.S.; Kaichev, V.V.; Kochubey, V.A.; Saraev, A.A.; Atuchin, V.V. X-ray photoelectron spectroscopy depth profiling of La_2O_3/Si thin films deposited by reactive magnetron sputtering. *ACS Appl. Mater. Interfaces* **2011**, *3*, 4370–4373.

18. Atuchin, V.V.; Molokeev, M.S.; Yurkin, G.Y.; Gavrilova, T.A.; Kesler, V.G.; Laptash, N.M.; Flerov, I.N.; Patrin, G.S. Synthesis, Structural, Magnetic, and Electronic Properties of Cubic $CsMnMoO_3F_3$ Oxyfluoride. *J. Phys. Chem. C* **2012**, *116*, 10162–10170, doi:10.1021/jp302020f.

19. Rubio, E.J.; Atuchin, V.V.; Kruchinin, V.N.; Pokrovsky, L.D.; Prosvirin, I.P.; Ramana, C.V. Electronic Structure and Optical Quality of Nanocrystalline Y_2O_3 Film Surfaces and Interfaces on Silicon. *J. Phys. Chem. C* **2014**, *118*, 13644–13651, doi:10.1021/jp502876r.

20. Atuchin, V.V.; Vinnik, D.; Gavrilova, T.A.; Gudkova, S.; Isaenko, L.I.; Jiang, X.; Pokrovsky, L.D.; Prosvirin, I.P.; Mashkovtseva, L.S.; Lin, Z. Flux Crystal Growth and the Electronic Structure of $BaFe_{12}O_{19}$ Hexaferrite. *J. Phys. Chem. C* **2016**, *120*, 5114–5123, doi:10.1021/acs.jpcc.5b12243.

21. Kang, L.; Lin, Z.; Qin, J.; Chen, C. Two novel nonlinear optical carbonates in the dee-ultraviolet region: $KBeCO_3F$ and $RbAlCO_3F_2$. *Sci. Rep.* **2013**, *3*, 1366.

22. Than, T.T.; Young, J.; Rondinelli, J.M.; Halasyamani, P.S. Mixed-metal carbonate fluorides as deep-ultraviolet non-linear optical materials. *J. Am. Chem. Soc.* **2017**, *139*, 1285–1295.

23. Zhang, X.; Wu, H.; Cheng, S.; Han, G.; Yang, Z.; Pan, S. $K_9[B_4O_5(OH)_4]_3(CO_3)X \times 7H_2O$ (X = Cl, Br): Synthesis, characterizations, and theoretical studies of noncentrosymmetric halogen borate-carbonates with short UV cutoff edges. *Inorg. Chem.* **2019**, *58*, 6974–6982.

24. Peng, G.; Lin, C.S.; Yang, Y.; Zhao, D.; Lin, Z.; Ye, N.; Huang, J.S. $Y_2(CO_3)_3 \times H_2O$ and $(NH_4)_2Ca_2Y_4(CO_3)_9 \times H_2O$: Partial aviovalent cation substitution enabling evolution from centrosymmetry to noncentrosymmetry for nonlinear optical response. *Chem. Mater.* **2019**, *31*, 52–56.

25. Chen, K.; Peng, G.; Lin, C.; Luo, M.; Fan, H.; Yang, S.; Ye, N. $NaPb_2(CO_3)_2F_2(OH)_{1-x}$ ($0 < x \leq 1$): A new member of alkali-lead carbonate fluoride system with large birefringence. *J. Solid State Chem.* **2020**, *288*, 121407, doi:10.1016/j.jssc.2020.121407.

26. Zou, G.; Ok, K.M. Novel ultraviolet (UV) nonlinear optical (NLO) materials discovered by chemical substitution-oriented design. *Chem. Sci.* **2020**, *11*, 5404–5409, doi:10.1039/d0sc01936d.

27. Gong, P.; Liu, X.; Kang, L.; Lin, Z. Inorganic planar p-conjugated groups in nonlinear optical crystals: Review and outlook. *Inorg. Chem. Front.* **2020**, *7*, 839–952.

28. Dorfman, S.M.; Badro, J.; Nabiei, F.; Prakapenka, V.B.; Cantoni, M.; Gillet, P. Carbonate stability in the reduced lower mantle. *Earth Planet. Sci. Lett.* **2018**, *489*, 84–91, doi:10.1016/j.epsl.2018.02.035.

29. Zolotoyabko, E.; Caspi, E.N.; Fieramosca, J.S.; Von Dreele, R.B.; Marin, F.; Mor, G.; Addadi, L.; Weiner, S.; Politi, Y. Differences between Bond Lengths in Biogenic and Geological Calcite. *Cryst. Growth Des.* **2010**, *10*, 1207–1214, doi:10.1021/cg901195t.

30. Liang, W.; Li, Z.; Yin, Y.; Li, R.; Chen, L.; He, Y.; Dong, H.; Dai, L.; Li, H. Single crystal growth, characterization and high-pressure Raman spectroscopy of impurity-free magnesite ($MgCO_3$). *Phys. Chem. Miner.* **2018**, *45*, 423–434, doi:10.1007/s00269-017-0930-1.

31. Liang, W.; Yin, Y.; Li, Z.; Li, R.; Li, L.; He, Y.; Dong, H.; Li, Z.; Yan, S.; Zhai, S.; et al. Single crystal growth, crystalline structure investigation and high-pressure behavior of impurity-free siderite ($FeCO_3$). *Phys. Chem. Miner.* **2018**, *45*, 831–842, doi:10.1007/s00269-018-0965-y.

32. Gao, J.; Zhu, F.; Lai, X.-J.; Huang, R.; Qin, S.; Chen, D.; Liu, J.; Zheng, L.-R.; Wu, X. Compressibility of a natural smithsonite $ZnCO_3$ up to 50 GPa. *High Press. Res.* **2014**, *34*, 89–99, doi:10.1080/08957959.2013.868454.

33. Liang, W.; Li, L.; Li, R.; Yin, Y.; Li, Z.; Liu, X.; Shan, S.; He, Y.; Meng, Y.; Li, Z.; et al. Crystal structure of impurity-free rhodochrosite ($MnCO_3$) and thermal expansion properties. *Phys. Chem. Miner.* **2020**, *47*, 1–11, doi:10.1007/s00269-019-01078-2.

34. Chariton, S.; Cerantola, V.; Ismailova, L.; Bykova, E.; Bykov, M.; Kupenko, I.; McCammon, C.; Dubrovinsky, L.S. The high-pressure behavior of spherocobaltite ($CoCO_3$): A single crystal Raman spectroscopy and XRD study. *Phys. Chem. Miner.* **2018**, *45*, 59–68, doi:10.1007/s00269-017-0902-5.

35. Reddy, B.J.; Frost, R.L. Electronic and vibrational spectra of gaspeite. *Neues Jahrb. Mineral. Mon.* **2004**, 525–536, doi:10.1127/0028-3649/2004/2004-0525.

36. Liu, L.G.; Lin, C.C. A Calcite → aragonite-type phase transition in $CdCO_3$. *Am. Mineral.* **1997**, *82*, 643–646, doi:10.2138/am-1997-5-625.

37. Liu, Z.T.Y.; Burton, B.P.; Khare, S.V.; Sarin, P. First-principles phase diagram calculations for the carbonate quasibinary systems $CaCO_3$-$ZnCO_3$, $CdCO_3$-$ZnCO_3$, $CaCO_3$-$CdCO_3$ and $MgCO_3$-$ZnCO_3$. *Chem. Geol.* **2016**, *443*, 137–145, doi:10.1016/j.chemgeo.2016.09.024.

38. Zucchini, A.; Comodi, P.; Nazzareni, S.; Hanfland, M. The effect of cation ordering and temperature on the high-pressure behaviour of dolomite. *Phys. Chem. Miner.* **2014**, *41*, 783–793, doi:10.1007/s00269-014-0691-z.

39. Garavelli, C.G.; Vurro, F.; Fioravanti, G.C. Minrecordite, a new mineral from Tsumeb. *Mineral. Rec.* **1982**, *13*, 131–136.

40. Chai, L.; Navrotsky, A. Synthesis, characterization, and energetics of solid solution along the dolomite-ankerite join, and implications for the stability of ordered $CaFe(CO_3)_2$. *Am. Mineral.* **1996**, *81*, 1141–1147, doi:10.2138/am-1996-9-1012.

41. Frondel, C.; Bauer, C.L.H. Kutnahorite: A manganese dolomite, CaMn(CO₃)₂. *Am. Mineral.* **1955**, *40*, 748–760.

42. Tareen, J.A.K.; Fazeli, A.R.; Basavalingu, B.; Bhandige, G.T. Decarbonation curves and associated thermodynamic data for synthetic Cd-dolomites CdMg(CO₃)₂, CdMn(CO₃)₂ and CdZn(CO₃)₂. *J. Therm. Anal.* **1995**, *44*, 937–954, doi:10.1007/bf02547277.

43. Bromiley, F.A.; Ballaran, T.B.; Langenhorst, F.; Seifert, F. Order and miscibility in the otavite-magnesite solid solution. *Am. Mineral.* **2007**, *92*, 829–836, doi:10.2138/am.2007.2315.

44. Effenberger, H.; Zemann, J. Single crystal X-ray investigation of norsethite, BaMg(CO₃)₂: One more mineral with an aplanar carbonate group. *Z. Krist.* **1985**, *171*, 275–280, doi:10.1524/zkri.1985.171.3-4.275.

45. Liang, W.; Li, L.; Yin, Y.; Li, R.; Li, Z.; Liu, X.; Zhao, C.; Yang, S.; Meng, Y.; Li, Z.; et al. Crystal structure of norsethite-type BaMn(CO₃)₂ and its pressure-induced transition investigated by Raman spectroscopy. *Phys. Chem. Miner.* **2019**, *46*, 771–781, doi:10.1007/s00269-019-01038-w.

46. Pippinger, T.; Miletich, R.; Effenberger, H.; Hofer, G.; Lotti, P.; Merlini, M. High-pressure polymorphism and structural transitions of norsethite, BaMg(CO₃)₂. *Phys. Chem. Miner.* **2014**, *41*, 737–755, doi:10.1007/s00269-014-0687-8.

47. Antao, S.M.; Hassan, I. The orthorhombic structure of CaCO₃, SrCO₃, PbCO₃ and BaCO₃: Linear structure trends. *Can. Mineral.* **2009**, *47*, 1245–1255, doi:10.3749/canmin.47.5.1245.

48. Ye, Y.; Smyth, J.R.; Boni, P. Crystal structure and thermal expansion of aragonite-group carbonates by single-crystal X-ray diffraction. *Am. Mineral.* **2012**, *97*, 707–712, doi:10.2138/am.2012.3923.

49. Kaabar, W.; Bott, S.; Devonshire, R. Raman spectroscopic study of mixed carbonate materials. *Spectrochim. Acta A* **2011**, *78*, 136–141, doi:10.1016/j.saa.2010.09.011.

50. Litasov, K.; Shatskiy, A.; Gavryushkin, P.N.; Bekhtenova, A.; Dorogokupets, P.I.; Danilov, B.S.; Higo, Y.; Akilbekov, A.T.; Inerbaev, T.M. P-V-T equation of state of CaCO₃ aragonite to 29 GPa and 1673 K: In situ X-ray diffraction study. *Phys. Earth Planet. Inter.* **2017**, *265*, 82–91, doi:10.1016/j.pepi.2017.02.006.

51. Lobanov, S.S.; Dong, X.; Martirosyan, N.S.; Samtsevich, A.I.; Stevanovic, V.; Gavryushkin, P.N.; Litasov, K.D.; Greenberg, E.; Prakapenka, V.B.; Oganov, A.R.; et al. Raman spectroscopy and x-ray diffraction of sp3CaCO3 at lower mantle pressures. *Phys. Rev. B* **2017**, *96*, 104101, doi:10.1103/physrevb.96.104101.

52. Smith, D.; Lawler, K.V.; Martinez-Canales, M.; Daykin, A.W.; Fussell, Z.; Smith, G.A.; Childs, C.; Smith, J.S.; Pickard, C.J.; Salamat, A. Postaragonite phases of CaCO₃ at lower mantle pressures. *Phys. Rev. Mater.* **2018**, *2*, 013605, doi:10.1103/physrevmaterials.2.013605.

53. Zhang, Z.; Mao, Z.; Liu, X.; Zhang, Y.; Brodholt, J.P. Stability and Reactions of CaCO₃ polymorphs in the Earth's Deep Mantle. *J. Geophys. Res. Solid Earth* **2018**, *123*, 6491–6500, doi:10.1029/2018jb015654.

54. Zhu, Y.; Li, Y.; Ding, H.; Lu, A.; Li, Y.; Wang, C. Infrared emission properties of a kind of natural carbonate: Interpretation from mineralogical analysis. *Phys. Chem. Miner.* **2020**, *47*, 1–15, doi:10.1007/s00269-020-01082-x.

55. Weir, C.E.; Lippincott, E.R. Infrared studies of aragonite, calcite, and vaterite type structures in the borates, carbonates, and nitrates. *J. Res. Natl. Bur. Stand. Sect. A Phys. Chem.* **1961**, *65*, 173–180, doi:10.6028/jres.065a.021.

56. Bischoff, W.D.; Sharma, S.K.; Mackenzie, F.T. Carbonate ion disorder in synthetic and biogenic magnesian calcites—A Raman spectral study. *Am. Mineral.* **1985**, *70*, 581–589.

57. Lin, C.-C.; Liu, L.-G. Post-aragonite phase transitions in strontianite and cerussite—A high pressure Raman spectroscopic study. *J. Phys. Chem. Solids* **1997**, *58*, 977–987, doi:10.1016/s0022-3697(96)00201-6.

58. Valenzano, L.; Noël, Y.; Orlando, R.; Zicovich-Wilson, C.M.; Ferrero, M.; Dovesi, R. Ab initio vibrational spectra and dielectric properties of carbonates: Magnesite, calcite and dolomite. *Theor. Chem. Acc.* **2007**, *117*, 991–1000, doi:10.1007/s00214-006-0213-2.

59. Kalinin, N.V.; Saleev, V.A. Ab initio modeling of Raman and infrared spectra of calcite. *Comput. Opt.* **2018**, *42*, 263–266, doi:10.18287/2412-6179-2018-42-2-263-266.

60. Sun, J.; Wu, Z.; Cheng, H.; Zhang, Z.; Frost, R.L. A Raman spectroscopic comparison of calcite and dolomite. *Spectrochim. Acta Part A Mol. Biomol. Spectrosc.* **2014**, *117*, 158–162, doi:10.1016/j.saa.2013.08.014.

61. Perrin, J.; Vielzeuf, D.; Laporte, D.; Ricolleau, A.; Rossman, G.R.; Floquet, N. Raman characterization of synthetic magnesian calcites. *Am. Mineral.* **2016**, *101*, 2525–2538, doi:10.2138/am-2016-5714.

62. Liu, J.; Caracas, R.; Fan, D.; Bobocioiu, E.; Zhang, D.; Mao, W.L. High-pressure compressibility and vibrational properties of (Ca,Mn)CO₃. *Am. Mineral.* **2016**, *101*, 2723–2730, doi:10.2138/am-2016-5742.

63. Minch, R.; Seoung, D.-H.; Ehm, L.; Winkler, B.; Knorr, K.; Peters, L.; Borkowski, L.; Parise, J.B.; Lee, Y.; Dubrovinsky, L.S.; et al. High-pressure behavior of otavite (CdCO3). *J. Alloy. Compd.* **2010**, *508*, 251–257, doi:10.1016/j.jallcom.2010.08.090.

64. Dufresne, W.J.; Rufledt, C.J.; Marshall, C.P. Raman spectroscopy of the eight natural carbonate minerals of calcite structure. *J. Raman Spectrosc.* **2018**, *49*, 1999–2007, doi:10.1002/jrs.5481.

65. Efthimiopoulos, I.; Germer, M.; Jahn, S.; Harms, M.; Reichmann, H.J.; Speziale, S.; Schade, U.; Sieber, M.; Koch-Müller, M. Effects of hydrostaticity on the structural stability of carbonates at lower mantle pressures: The case study of dolomite. *High Press. Res.* **2018**, *39*, 36–49, doi:10.1080/08957959.2018.1558223.

66. Efthimiopoulos, I.; Jahn, S.; Kuras, A.; Schade, U.; Koch-Müller, M. Combined high-pressure and high-temperature vibrational studies of dolomite: Phase diagram and evidence of a new distorted modification. *Phys. Chem. Miner.* **2017**, *44*, 465–476, doi:10.1007/s00269-017-0874-5.

67. Martens, W.N.; Rintoul, L.; Kloprogge, J.T.; Frost, R.L. Single crystal raman spectroscopy of cerussite. *Am. Mineral.* **2004**, *89*, 352–358, doi:10.2138/am-2004-2-314.

68. Wang, X.; Ye, Y.; Wu, X.; Smyth, J.R.; Yang, Y.; Zhang, Z.; Wang, Z. High-temperature Raman and FTIR study of aragonite-group carbonates. *Phys. Chem. Miner.* **2018**, *46*, 51–62, doi:10.1007/s00269-018-0986-6.

69. Efthimiopoulos, I.; Müller, J.; Winkler, B.; Otzen, C.; Harms, M.; Schade, U.; Koch-Müller, M. Vibrational response of strontianite at high pressures and high temperatures and construction of P–T phase diagram. *Phys. Chem. Miner.* **2019**, *46*, 27–35, doi:10.1007/s00269-018-0984-8.

70. Lane, M.D.; Christensen, P.R. Thermal infrared emission spectroscopy of anhydrous carbonates. *J. Geophys. Res.* **1997**, *102*, 25581–25592, doi:10.1029/97je02046.

71. Deines, P. Carbon isotope effects in carbonate systems. *Geochim. Cosmochim. Acta* **2004**, *68*, 2659–2679, doi:10.1016/j.gca.2003.12.002.

72. Brusentsova, T.N.; Peale, R.E.; Maukonen, D.; Harlow, G.E.; Boesenberg, J.S.; Ebel, D.; Prêt, D.; Sammartino, S.; Beaufort, D.; Fialin, M.; et al. Far infrared spectroscopy of carbonate minerals. *Am. Mineral.* **2010**, *95*, 1515–1522, doi:10.2138/am.2010.3380.

73. Farsang, S.; Facq, S.; Redfern, S.A.T. Raman modes of carbonate minerals as pressure and temperature gauges up to 6 GPa and 500 °C. *Am. Mineral.* **2018**, *103*, 1988–1998, doi:10.2138/am-2018-6442.

74. Erba, A.; Baima, J.; Bush, I.; Orlando, R.; Dovesi, R. Large-Scale Condensed Matter DFT Simulations: Performance and Capabilities of the CRYSTAL Code. *J. Chem. Theory Comput.* **2017**, *13*, 5019–5027, doi:10.1021/acs.jctc.7b00687.

75. Dovesi, R.; Erba, A.; Orlando, R.; Zicovich-Wilson, C.M.; Civalleri, B.; Maschio, L.; Rérat, M.; Casassa, S.; Baima, J.; Salustro, S.; et al. Quantum-mechanical condensed matter simulations with CRYSTAL. *Wiley Interdiscip. Rev. Comput. Mol. Sci.* **2018**, *8*, e1360, doi:10.1002/wcms.1360.

76. Becke, A.D. Density functional thermochemistry. III. The role of exact exchange. *J. Chem. Phys.* **1993**, *98*, 5648–5652, doi:10.1063/1.464913.

77. Lee, C.; Yang, W.; Parr, R.G. Development of the Colle-Salvetti correlation-energy formula into a functional of the electron density. *Phys. Rev. B* **1988**, *37*, 785–789, doi:10.1103/physrevb.37.785.

78. Valenzano, L.; Torres, F.J.; Doll, K.; Pascale, F.; Zicovich-Wilson, C.M.; Dovesi, R. Ab InitioStudy of the Vibrational Spectrum and Related Properties of Crystalline Compounds; the Case of CaCO3Calcite. *Z. Phys. Chem.* **2006**, *220*, 893–912, doi:10.1524/zpch.2006.220.7.893.

79. Peintinger, M.F.; Oliveira, D.V.; Bredow, T. Consistent Gaussian basis sets of triple-zeta valence with polarization quality for solid-state calculations. *J. Comput. Chem.* **2013**, *34*, 451–459, doi:10.1002/jcc.23153.

80. Laun, J.; Oliveira, D.V.; Bredow, T. Consistent gaussian basis sets of double- and triple-zeta valence with polarization quality of the fifth period for solid-state calculations. *J. Comput. Chem.* **2018**, *39*, 1285–1290, doi:10.1002/jcc.25195.

81. Piskunov, S.; Heifets, E.; Eglitis, R.; Borstel, G. Bulk properties and electronic structure of SrTiO3, BaTiO3, PbTiO3 perovskites: An ab initio HF/DFT study. *Comput. Mater. Sci.* **2004**, *29*, 165–178, doi:10.1016/j.commatsci.2003.08.036.

82. Evarestov, R.; Kotomin, E.A.; Mastrikov, Y.; Gryaznov, D.; Heifets, E.; Maier, J. Comparative density-functional LCAO and plane-wave calculations ofLaMnO3surfaces. *Phys. Rev. B* **2005**, *72*, 214411, doi:10.1103/physrevb.72.214411.

83. Sophia, G.; Baranek, P.; Sarrazin, C.; Rérat, M.; Dovesi, R. First-principles study of the mechanisms of the pressure-induced dielectric anomalies in ferroelectric perovskites. *Phase Transit.* **2013**, *86*, 1069–1084, doi:10.1080/01411594.2012.754442.

84. Monkhorst, H.J.; Pack, J.D. Special points for Brillouin-zone integrations. *Phys. Rev. B* **1976**, *13*, 5188, doi:10.1103/physrevb.13.5188.

85. Pascale, F.; Zicovich-Wilson, C.M.; Gejo, F.L.; Civalleri, B.; Orlando, R.; Dovesi, R. The calculation of the vibrational frequencies of crystalline compounds and its implementation in the CRYSTAL code. *J. Comput. Chem.* **2004**, *25*, 888–897, doi:10.1002/jcc.20019.

86. Zicovich-Wilson, C.M.; Pascale, F.; Roetti, C.; Saunders, V.R.; Orlando, R.; Dovesi, R. Calculation of the vibration frequencies of alpha-quartz: The effect of Hamiltonian and basis set. *J. Comput. Chem.* **2004**, *25*, 1873–1881, doi:10.1002/jcc.20120.

87. Carteret, C.; De La Pierre, M.; Dossot, M.; Pascale, F.; Erba, A.; Dovesi, R. The vibrational spectrum of $CaCO_3$ aragonite: A combined experimental and quantum-mechanical investigation. *J. Chem. Phys.* **2013**, *138*, 014201, doi:10.1063/1.4772960.

88. Baima, J.; Ferrabone, M.; Orlando, R.; Erba, A.; Dovesi, R. Thermodynamics and phonon dispersion of pyrope and grossular silicate garnets from ab initio simulations. *Phys. Chem. Miner.* **2016**, *43*, 137–149, doi:10.1007/s00269-015-0781-6.

89. Maschio, L.; Kirtman, B.; Rérat, M.; Orlando, R.; Dovesi, R. Ab initio analytical Raman intensities for periodic systems through a coupled perturbed Hartree-Fock/Kohn-Sham method in an atomic orbital basis. II. Validation and comparison with experiments. *J. Chem. Phys.* **2013**, *139*, 164102, doi:10.1063/1.4824443.

90. Korabel'Nikov, D.; Zhuravlev, Y.N. Structural, elastic, electronic and vibrational properties of a series of sulfates from first principles calculations. *J. Phys. Chem. Solids* **2018**, *119*, 114–121, doi:10.1016/j.jpcs.2018.03.037.

91. Shannon, R.D. Revised effective ionic radii and systematic studies of interatomic distances in halides and chalcogenides. *Acta Crystallogr. Sect. A* **1976**, *32*, 751–767, doi:10.1107/s0567739476001551.

92. Grzechnik, A.; Simon, P.; Gillet, P.; McMillan, P. An infrared study of $MgCO_3$ at high pressure. *Phys. B Condens. Matter* **1999**, *262*, 67–73, doi:10.1016/s0921-4526(98)00437-2.

93. Clark, S.J.; Jouanna, P.; Haines, J.; Mainprice, D. Calculation of infrared and Raman vibration modes of magnesite at high pressure by density-functional perturbation theory and comparison with experiments. *Phys. Chem. Miner.* **2010**, *38*, 193–202, doi:10.1007/s00269-010-0395-y.

94. Yao, C.; Wu, Z.; Zou, F.; Sun, W. Thermodynamic and Elastic Properties of Magnesite at Mantle Conditions: First-Principles Calculations. *Geochem. Geophys. Geosystems* **2018**, *19*, 2719–2731, doi:10.1029/2017gc007396.

95. Gillet, P.; Biellmann, C.; Reynard, B.; McMillan, P. Raman spectroscopic studies of carbonates part I: High-pressure and high-temperature behaviour of calcite, magnesite, dolomite and aragonite. *Phys. Chem. Miner.* **1993**, *20*, 1–18, doi:10.1007/bf00202245.

96. Schauble, E.A.; Ghosh, P.; Eiler, J.M. Preferential formation of 13C–18O bonds in carbonate minerals, estimated using first-principles lattice dynamics. *Geochim. Cosmochim. Acta* **2006**, *70*, 2510–2529, doi:10.1016/j.gca.2006.02.011.

97. De La Pierre, M.; Carteret, C.; Maschio, L.; André, E.; Orlando, R.; Dovesi, R. The Raman spectrum of CaCO3 polymorphs calcite and aragonite: A combined experimental and computational study. *J. Chem. Phys.* **2014**, *140*, 164509, doi:10.1063/1.4871900.

98. Spivak, A.V.; Solopova, N.; Cerantola, V.; Bykova, E.; Zakharchenko, E.; Dubrovinsky, L.S.; Litvin, Y. Raman study of $MgCO_3$–$FeCO_3$ carbonate solid solution at high pressures up to 55 GPa. *Phys. Chem. Miner.* **2014**, *41*, 633–638, doi:10.1007/s00269-014-0676-y.

99. Siva, T.; Muralidharan, S.; Sathiyanarayanan, S.; Manikandan, E.; Jayachandran, M. Enhanced Polymer Induced Precipitation of Polymorphous in Calcium Carbonate: Calcite Aragonite Vaterite Phases. *J. Inorg. Organomet. Polym. Mater.* **2017**, *27*, 770–778, doi:10.1007/s10904-017-0520-1.

100. Farfan, G.A.; Boulard, E.; Wang, S.; Mao, W.L. Bonding and electronic changes in rhodochrosite at high pressure. *Am. Mineral.* **2013**, *98*, 1817–1823, doi:10.2138/am.2013.4497.

101. Zhao, C.; Li, H.; Jiangb, J.; He, Y.; Liang, W. Phase Transition and vibration properties of $MnCO_3$ at high pressure and high-temperature by Raman spectroscopy. *High Press. Res.* **2018**, *38*, 212–223, doi:10.1080/08957959.2018.1476505.

102. Böttcher, M.E.; Gehlken, P.-L.; Skogby, H.; Reutel, C. The vibrational spectra of $BaMg(CO_3)_2$ (norsethite). *Miner. Mag.* **1997**, *61*, 249–256, doi:10.1180/minmag.1997.061.405.08.

103. Chaney, J.; Santillán, J.D.; Knittle, E.; Williams, Q. A high-pressure infrared and Raman spectroscopic study of $BaCO_3$: The aragonite, trigonal and Pmmn structures. *Phys. Chem. Miner.* **2015**, *42*, 83–93, doi:10.1007/s00269-014-0702-0.

104. Brooker, M.H.; Sunder, S.; Taylor, P.; Lopata, V.J. Infrared and Raman spectra and X-ray diffraction studies of solid lead(II) carbonates. *Can. J. Chem.* **1982**, *61*, 494–502, doi:10.1139/v83-087.

105. Catalli, K.; Santillán, J.; Williams, Q. A high pressure infrared spectroscopic study of $PbCO_3$-cerussite: Constraints on the structure of the post-aragonite phase. *Phys. Chem. Miner.* **2005**, *32*, 412–417, doi:10.1007/s00269-005-0010-9.

106. Frech, R.; Wang, E.C.; Bates, J.B. The i.r. and Raman spectra of $CaCO_3$ (aragonite). *Spectrochim. Acta Part A Mol. Spectrosc.* **1980**, *36*, 915–919, doi:10.1016/0584-8539(80)80044-4.

107. Bayarjargal, L.; Fruhner, C.-J.; Schrodt, N.; Winkler, B. $CaCO_3$ phase diagram studied with Raman spectroscopy at pressures up to 50 GPa and high temperatures and DFT modeling. *Phys. Earth Planet. Inter.* **2018**, *281*, 31–45, doi:10.1016/j.pepi.2018.05.002.

108. Biedermann, N.; Speziale, S.; Winkler, B.; Reichmann, H.J.; Koch-Müller, M.; Heide, G. High-pressure phase behavior of $SrCO_3$: An experimental and computational Raman scattering study. *Phys. Chem. Miner.* **2017**, *44*, 335–343, doi:10.1007/s00269-016-0861-2.

109. Minch, R.; Dubrovinsky, L.S.; Kurnosov, A.; Ehm, L.; Knorr, K.; Depmeier, W. Raman spectroscopic study of $PbCO_3$ at high pressures and temperatures. *Phys. Chem. Miner.* **2010**, *37*, 45–56, doi:10.1007/s00269-009-0308-0.

110. Alía, J.M.; de Mera, Y.D.; Edwards, H.G.M.; Martín, P.G.; Andres, S.L. FT-Raman and infrared spectroscopic study of aragonite-strontianite $(Ca_xSr_{1-x}CO_3)$ solid solution. *Spectrochim. Acta Part A Mol. Biomol. Spectrosc.* **1997**, *53*, 2347–2362, doi:10.1016/s1386-1425(97)00175-3.